Dependence of T_c of YBa$_2$Cu$_3$O$_{6.67}$ on in-plane uniaxial stress

Mark E. Barber [1,*] Hun-ho Kim,[2] Toshinao Loew,[2] Matthieu Le Tacon [3] Matteo Minola [2] Marcin Konczykowski [4]

Bernhard Keimer [2] Andrew P. Mackenzie [1,5] and Clifford W. Hicks[1,6,†]

[1]*Max Planck Institute for Chemical Physics of Solids, Nöthnitzer Straße 40, 01187 Dresden, Germany*

[2]*Max Planck Institute for Solid State Research, Heisenbergstraße 1, 70569 Stuttgart, Germany*

[3]*Karlsruhe Institute of Technology, Institute for Quantum Materials and Technologies,*
Hermann-von-Helmholtz-Platz 1, 76344 Eggenstein-Leopoldshafen, Germany

[4]*Laboratoire des Solides Irradiés, CEA/DRF/lRAMIS, Ecole Polytechnique, CNRS,*
Institut Polytechnique de Paris, F-91128 Palaiseau, France

[5]*Scottish Universities Physics Alliance, School of Physics and Astronomy,*
University of St. Andrews, St. Andrews KY16 9SS, United Kingdom

[6]*School of Physics and Astronomy, University of Birmingham, Birmingham B15 2TT, United Kingdom*

We probe the effect on T_c of in-plane uniaxial stress applied to the high-temperature superconductor YBa$_2$Cu$_3$O$_{6.67}$. We find a highly anisotropic response. Under compression along the b axis, which reduces the orthorhombicity of the CuO$_2$ planes, T_c is broadly flat for stresses up to at least 1.7 GPa. Under compression along the a axis, T_c decreases steeply. For stresses beyond ≈ 1 GPa the decrease is quasilinear. We hypothesize that superconductivity is suppressed by competition with uniaxial charge density wave order, which has been found to onset at ≈ 1 GPa.

I. INTRODUCTION

The effect of lattice distortion on superconductivity can provide information on superconducting mechanisms. For the unconventional superconductor Sr$_2$RuO$_4$, a dramatic enhancement in T_c and H_{c2} at a uniaxial stress-induced Lifshitz transition shows that the Fermi-level density of states is crucial, and constrains the symmetry of possible order parameters [1]. For optimally-doped YBa$_2$Cu$_3$O$_{6+x}$, thermal expansion [2] and uniaxial stress measurements [3] show that weaker orthorhombicity favors the superconductivity. In recent years, it has become possible to apply uniaxial stresses of up to ≈ 2 GPa to correlated electron materials while remaining in the elastic limit [4]. With stresses on this scale, it is realistic for applied stress to overcome the orthorhombicity of the YBa$_2$Cu$_3$O$_{6+x}$ crystal structure and impose the condition $a = b$, where a and b are the in-plane lattice constants. It is realistic to go beyond the first-order terms in the stress dependence and explore T_c as a function of applied lattice orthorhombicity.

Here, we report measurements on YBa$_2$Cu$_3$O$_{6.67}$, where the doping is $\approx 1/8$ per site in the CuO$_2$ plane. We choose this doping because the presence of charge order at this doping, and its apparent competition with the superconductivity, may cause a stronger response of the superconductivity to lattice distortion than at other dopings. In unstressed YBa$_2$Cu$_3$O$_{6.67}$, charge order appears that has weak interlayer correlation, and that is therefore referred to as the 2D charge order [5,6]. It weakens when superconductivity appears, indicating that these phases compete [5,7,8]. Under compression along the a axis a form of charge order appears that has much longer correlation along the c axis; it is referred to as the 3D charge order [9]. While the 2D charge order is comprised of domains with modulation along the a and b axes [10], the 3D charge order develops modulation along only the b axis [11].

The evidence on competition between the 3D charge order and superconductivity is ambiguous. The 3D charge order can be induced in unstressed samples by magnetic field [11–13], and coexists with superconductivity for fields above $\approx 0.7 H_{c2}$ [13,14]. However, the presence of vortex cores makes it difficult to draw firm conclusions on whether this coexistence is intrinsic. In scanning tunneling microscopy on Bi$_2$Sr$_2$CaCu$_2$O$_{8+x}$, charge order is observed within the vortex cores, suggesting that it appears only where superconductivity is suppressed [15,16]. In YBa$_2$Cu$_3$O$_{6.67}$, the in-plane correlation length of the 3D charge order exceeds the intervortex spacing, and it has been argued that the interaction between vortex halos is too weak for this to occur without long-range, microscopic coexistence [17]. The key advantage in using uniaxial stress rather than magnetic field to induce the 3D charge order is that the intrinsic inhomogeneity of the mixed phase

---

*Present address: Department of Applied Physics and Geballe Laboratory for Advanced Materials, Stanford University, Stanford, California 94305, USA; mebarber@stanford.edu
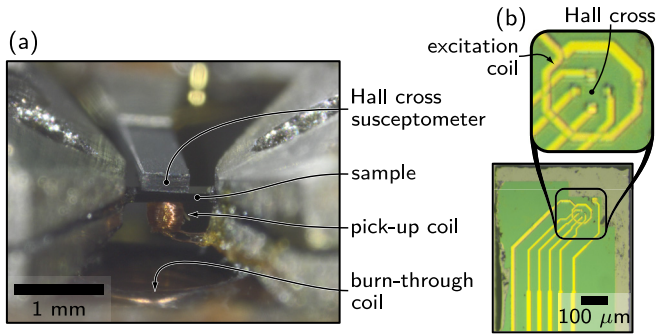
†c.hicks.1@bham.ac.uk

FIG. 1. (a) A photograph of sample 2, mounted for measurement. (b) The tip of the Hall cross susceptometer. The Hall cross is fabricated from a GaAs/AlGaAs 2D electron gas heterostructure. The cross itself is defined by proton irradiation, and is not visible.

is avoided. Under *a*-axis compression, the 3D charge order disappears at low temperature [9], which suggests that it does not coexist with the superconductivity, but that interpretation would be strengthened by identification of a reciprocal effect of the 3D charge order on the superconductivity.

II. METHODS

We use a piezoelectric-driven uniaxial stress cell that incorporates a sensor of the force applied to the sample. This allows the applied stress to be accurately measured even if the epoxy holding the sample deforms nonelastically, which is a concern for sample stresses larger than ≈ 1 GPa [4]. A photograph of sample 2 is shown in Fig. 1(a). The central, exposed portion of the sample is about 1 mm in length. T_c is measured using a microfabricated susceptometer [18], comprising a 10×10 μm^2 Hall cross surrounded by a 70-μm-diameter excitation coil [see Fig. 1(b)]. By measuring over a small length scale, averaging over sample inhomogeneity is minimized [19]. To aid flux motion through the sample, a "burn-through" field of ≈ 200 μT, 20 kHz was applied during measurement using a separate coil. This step was necessary because in samples with short-length-scale T_c inhomogeneity, Josephson coupling between regions with higher T_c can hinder flux motion if the probing field is weak, giving the appearance of a bulk Meissner effect above the true bulk T_c [20]. Finally, our setup includes a separate pick-up coil that, in combination with the burn-through coil, can be used for long-length-scale measurements of T_c.

Three samples were cut from the same single, detwinned crystal of $YBa_2Cu_3O_{6.67}$, with $T_c \approx 65$ K: sample 1 for application of stress along the *b* axis, and samples 2 and 3 along the *a* axis. All had approximately the same dimensions. Large stress was applied only at temperatures below 100 K, to avoid altering the oxygen order in the chain layers [21,22]. The stress was periodically released and measurements repeated at smaller stress to check for alteration of the superconducting transition by application of high stress, but no such effects were observed.

For sample 3, a thermocouple was also affixed to the sample for measurement of the elastocaloric effect. The elastocaloric effect is the strain-induced change in sample temperature under adiabatic conditions. It is measured by
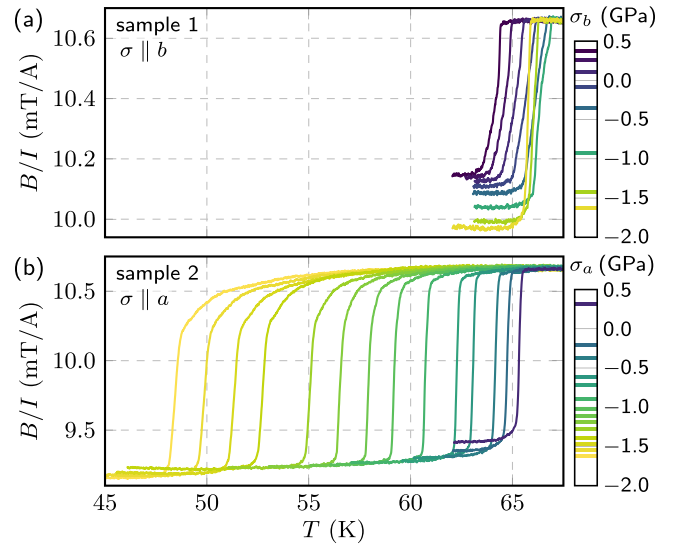

FIG. 2. Raw data. (a) The real part of the susceptometer response B/I (field in the Hall cross divided by current in the excitation coil) vs temperature for sample 1 at various *b*-axis pressures σ_b. The field from the excitation coil of the susceptometer at the sample surface is ≈ 25 μT, 211 Hz. $\sigma < 0$ denotes compression. (b) B/I vs T for sample 2 at various σ_a.

applying an ac strain, at a frequency low enough that the thermocouple thermalizes to the sample, but high enough that the exposed portion of the sample does not thermalize to the stress cell [23]. Our measurement frequency was 23 Hz, at which the thermal diffusion length is ≈ 500 μm for temperatures between 40 and 60 K [24].

III. RESULTS

Figure 2 shows raw susceptibility data from samples 1 and 2 at various stresses. The plotted data are B/I, where B is the field measured in the Hall cross in response to current I applied to the excitation coil. The superconducting transitions remain narrow up to the highest stresses reached, even for sample 2 where T_c shifts rapidly with the applied stress. These narrow transitions show that good strain homogeneity was obtained over the region sensed by the Hall cross susceptometer. We take T_c as the temperature where the slope $d(B/I)/dT$ is largest.

As sample 2 was compressed, strong tails did appear on the high-temperature side of the transitions. Strain inhomogeneity will affect measurements of T_c more at strains where $|dT_c/d\sigma|$ is larger; σ is applied stress. The effect of sample inhomogeneity may also be magnified at larger stresses, for example if slightly different dopings lead to different onset stresses of the 3D charge order. As shown in Fig. 3, samples 2 and 3 have nearly the same T_c at zero applied stress, but their T_c's differ by ≈ 4 K at $\sigma_a = -1.5$ GPa (where σ_a is stress applied along the *a* axis and negative values denote compression).

T_c data from all three samples are shown together in Fig. 3(a). $dT_c/d\sigma_a$ and $dT_c/d\sigma_b$ at $\sigma_a = \sigma_b = 0$ have opposite signs, which shows that the orthorhombicity $a - b$ affects T_c more strongly than the in-plane unit cell area $a \times b$ or the *c*-axis lattice constant (both of which also vary under uniaxial
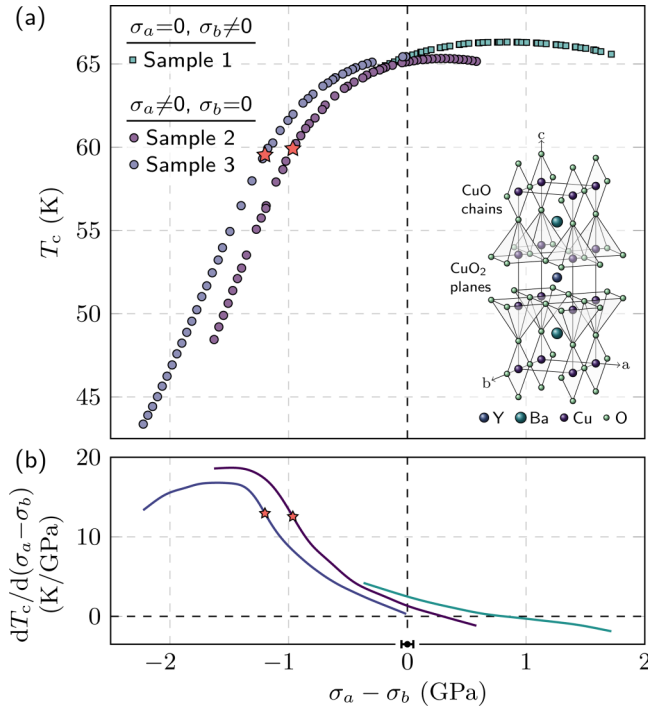
FIG. 3. (a) Dependence of T_c on uniaxial stress, applied along the b axis for sample 1, and the a axis for samples 2 and 3. T_c is taken as the temperature of maximum $d(B/I)/dT$; see Fig. 2. (b) Derivatives $dT_c/d(\sigma_a - \sigma_b)$, obtained from quintic smoothing splines of the data in panel (a). T_c is seen to depend approximately quadratically on $\sigma_a - \sigma_b$ for $\sigma_a - \sigma_b$ greater than ≈ -1.0 GPa, and approximately linearly for $\sigma_a - \sigma_b$ less than ≈ -1.3 GPa. The stars mark the stresses, for samples 2 and 3, where $|d^2 T_c / d\sigma_a^2|$ is maximum. The inset of panel (a) shows the lattice structure of $YBa_2Cu_3O_7$.

stress). To emphasize the role of the orthorhombicity, we plot T_c of all three samples together against $\sigma_a - \sigma_b$.

We observe $dT_c/d\sigma_b|_{\sigma_b=0} = -2.5$ K/GPa for sample 1, and $dT_c/d\sigma_a|_{\sigma_a=0} = +1.3$ and $+0.3$ K/GPa for samples 2 and 3, respectively. These are comparable to previous results on $YBa_2Cu_3O_{6.75}$ [3]: $dT_c/d\sigma_b|_{\sigma_b=0} = -2.4$ K/GPa and $dT_c/d\sigma_a|_{\sigma_a=0} = +1.6$ K/GPa. Under compression along the b axis, T_c increases and reaches a maximum at $\sigma_b = -0.8$ GPa. This is not the stress where $a = b$: based on lattice constant and elastic modulus data reported in Refs. [25,26], $a = b$ at $\sigma_b \approx -1.6$ GPa. However, because of the presence of the CuO chain layer, and because uniaxial stress does also alter the c lattice constant and the unit cell area $a \times b$, T_c is not expected to be precisely symmetric about the point where $a = b$. The overall quadratic dependence of T_c on b-axis compression suggests that a tetragonal lattice does generally favor superconductivity.

For weak a-axis compression, this quadratic dependence on lattice orthorhombicity appears to continue, but then for σ_a below about -1 GPa the dependence of T_c on stress becomes much steeper. It also becomes quasilinear. In Fig. 3(b), we show the derivative $dT_c/d(\sigma_a - \sigma_b)$, which is seen to flatten for $\sigma_a < -1.3$ GPa. In Figs. 3(a) and 3(b), we highlight with stars the points where the second derivative is largest, and identify these as the crossover stresses between quasiquadratic and quasilinear dependence of T_c on uniaxial stress. $dT_c^2/d\sigma_a^2$
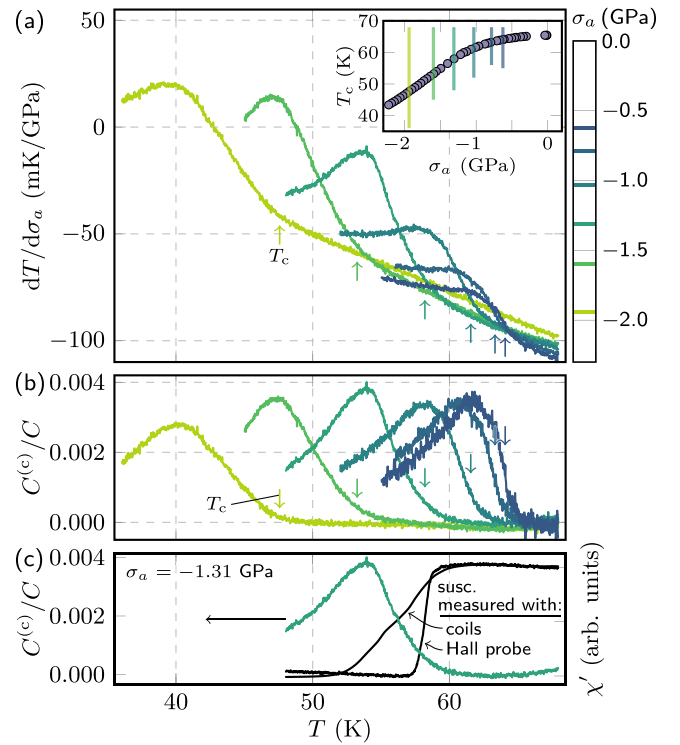

FIG. 4. (a) Elastocaloric effect data—the change in temperature with applied stress under quasiadiabatic conditions—from sample 3. The inset shows the location of each ramp against the $T_c(\sigma_a)$ curve. Arrows in the main panel indicate T_c, as measured with the Hall cross susceptometer. (b) A normalization of the data in (a), described in the text. $C^{(c)}/C$ is the critical part of the heat capacity divided by the total heat capacity. (c) Comparison of ECE data at -1.31 GPa with susceptibility measured with the Hall cross susceptometer, and with the combination of pick-up and burn-through coils.

is largest at $\sigma_a = -0.97$ GPa for sample 2, and -1.2 GPa for sample 3.

We now report data on the heat capacity anomaly at T_c, measured on sample 3 through the elastocaloric effect (ECE). The measurement conditions are given in the Appendix. Raw data—the rate of change of T with uniaxial stress σ_a—are shown in Fig. 4(a). The data show broad step- or peak-like features that approximately track T_c.

To analyze these data, we employ the model of Ref. [23], in which the total heat capacity C is taken to be $C^{(nc)} + C^{(c)}$, where $C^{(c)}$ is the portion of the heat capacity that moves with the superconducting transition, and $C^{(nc)}$ is a noncritical background. $C^{(c)}$ is taken to have the form $C^{(c)}(T, \sigma) = C^{(c)}(T - T_c(\sigma))$. In this model, and in the adiabatic limit,

$$\frac{dT}{d\sigma} = \frac{C^{(c)}}{C} \frac{dT_c}{d\sigma} + \frac{dT^{(nc)}}{d\sigma},$$

where $dT^{(nc)}/d\sigma$ is the contribution from noncritical changes in entropy [23]. To obtain $C^{(c)}/C$, we first subtract a common slope from all of the curves in Fig. 4(a), as an estimate for $dT^{(nc)}/d\sigma$. We then divide each curve by $0.8 \times dT_c/d\sigma_a$, taking $dT_c/d\sigma_a$ at each stress from the data shown in Fig. 3(b). The factor of 0.8 accounts for the fact that the measurement is not fully in the adiabatic limit; see the Appendix for details.

Results are shown in Fig. 4(b). $C^{(c)}$ is found to peak at $\approx 0.4\%$ of the total heat capacity, in good agreement with direct measurement at zero stress [27]. The location of the peak in $C^{(c)}$ tracks T_c. The maximum in $C^{(c)}/C$ remains broadly constant at $\approx 0.4\%$ as stress is applied, even over the stress range $\sigma_a < -1$ GPa where T_c decreases steeply.

The peaks in $C^{(c)}$ are broader than the superconducting transitions shown in Fig. 2, and in Fig. 4(c), we show that this is at least in part a consequence of the fact that the ECE measurements average over a larger portion of the sample than the susceptibility measurements using the Hall cross susceptometer. We show in Fig. 4(c) the ECE data at $\sigma_a = -1.31$ GPa, along with the susceptibility as measured both with the susceptometer and with the combination of pick-up and burn-through coils, which as already noted average over more of the sample than the susceptometer. The superconducting transition as seen in the coils is much broader than that seen with the Hall sensor, and matches well the location and breadth of the transition seen in the ECE data. Greater strain inhomogeneity, due to the larger spatial extent of the measurement, could be a contributor to the larger transition width, but long-length-scale sample inhomogeneity could also be important. At $\sigma_a = -1.31$ GPa, the transition width as seen with the burn-through and pick-up coils is ≈ 6 K. The difference between T_c of samples 2 and 3, which were cut from the same original crystal, at -1.31 GPa is comparable: ≈ 3 K.

IV. DISCUSSION

We have observed a strongly asymmetric response of T_c to in-plane uniaxial stress in YBa$_2$Cu$_3$O$_{6.67}$: under compression up to $\sigma_b = -1.7$ GPa along the b axis, T_c changes by only a few kelvin, while under compression along the a axis by $\sigma_a \approx -1.7$ GPa T_c decreases by about 20 K.

We discuss first a hypothesis that this decrease is driven primarily by competition with charge order. In a competing-order model of T_c, the applied stress can affect T_c through direct coupling to the pairing, competition with the 2D charge order, or competition with the 3D charge order. At small $|\sigma_a|$, both the superconductivity and 2D charge order are expected to have a dominantly quadratic coupling to lattice orthorhombicity $a - b$, though with an offset due to the chains. d-wave superconductivity on the CuO$_2$ planes is symmetric with respect to compression along the a versus the b axes. The 2D charge order also responds in a qualitatively symmetric way to a- versus b-axis compression: compression along the a axis strengthens the b-oriented modulation, and vice versa [10]. The 3D charge order, on the other hand, is a uniaxial order, with modulation along the b but not the a axis. Its magnitude is therefore expected to couple linearly to $a - b$, and so competition with this order would drive a stress-linear decrease in T_c. Furthermore, the crossover stress between stress-quadratic and stress-linear behavior is consistent with the onset stress of the 3D charge order observed in x-ray data. In Ref. [9], 3D charge order was reported to onset, at 50 K, at an a-axis strain of between -0.8 and -1.0×10^{-2}, though Bragg reflection data in that publication indicates that the onset strain could have been as small as -0.6×10^{-2}. In Ref. [10], 3D charge order was also found to onset, at 55 K, at an a-axis strain between -0.6 and -1.0×10^{-2}. The

room-temperature a-axis Young's modulus of YBa$_2$Cu$_3$O$_{7-x}$ is ≈ 160 GPa [26]. Applying this Young's modulus, a strain range of -0.6 to -1.0×10^{-2} corresponds to a stress range of -1.0 to -1.6 GPa.

An alternative hypothesis is that the stress dependence of T_c is dominated by stress-driven changes in electronic structure, such as charge transfer between the chains and planes, a change in coupling between the planes, or something else. In studies under hydrostatic stress, a rate of charge transfer of ~ 0.01 holes/GPa has been found [28,29] (though Ref. [30] argues for a lower rate). At a doping of 1/8 holes per Cu, a charge transfer rate of 0.01 holes/GPa would yield $dT_c/dP \sim 8$ K/GPa [31], where P is hydrostatic pressure. This is in the range of the uniaxial stress effects observed here, although measurements under uniaxial stress at other dopings suggest that it is c-axis stress rather than in-plane stress that is the main driver of charge transfer: $dT_c/d\sigma_c$ changes sign at optimal doping, while the effect of in-plane stress does not show any such sign change [3]. Stress-driven changes in interlayer coupling may also be important: in electronic structure calculations for optimally doped YBa$_2$Cu$_3$O$_{6+x}$, in-plane stress was found to drive little chain-plane charge transfer but a substantial change in the coupling between the planes of the CuO$_2$ bilayers [32].

We argue that competition with charge order is the more likely of these two hypotheses, because it can straightforwardly explain the steep stress-linear decrease in T_c, while reproducing this feature with charge transfer or other changes in electronic structure would require some tuning. This competition hypothesis is consistent with the results of Ref. [33], in which it is reported that when field is applied to unstressed YBa$_2$Cu$_3$O$_{6.67}$ the superconductivity weakens faster in regions of the sample where the 3D charge order appears first. However, the causation there is unclear: onset of the 3D charge order could have suppressed the superconductivity, or the 3D charge order could have appeared first in regions of the sample where the superconductivity was already weaker. An anomaly in $T_c(\sigma_a)$ at the onset stress of 3D charge order is a more definitive indication that the charge order affects the superconductivity. We note though that if the superconductivity and 3D charge order did compete strongly, a smaller heat capacity anomaly at T_c is in general expected under large $|\sigma_a|$, where the transition into superconductivity is from the 3D charge order state. This is because the 3D charge order would suppress some of the entropy that drives the superconductivity. This point should be investigated further.
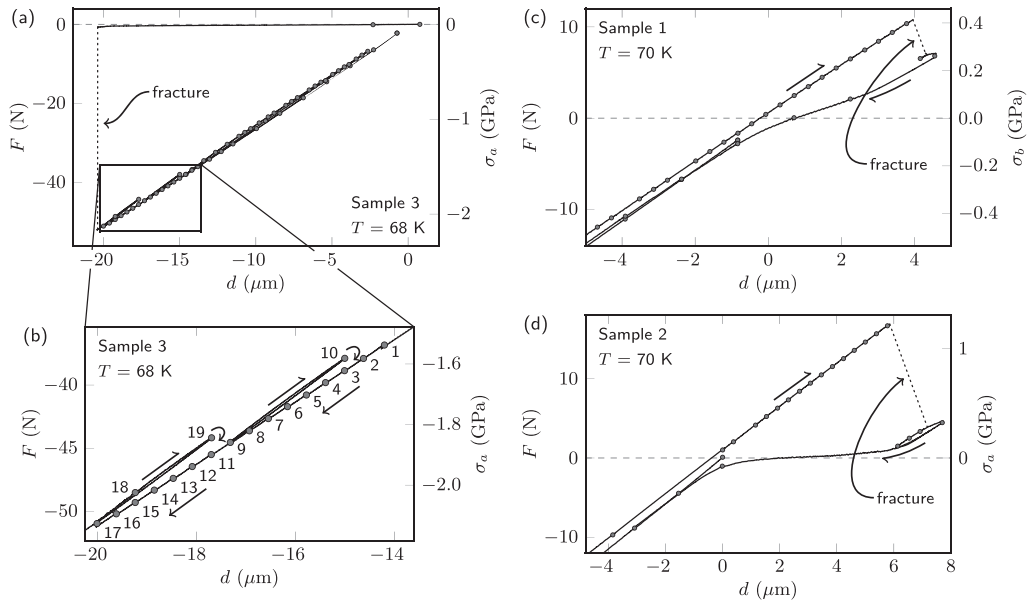
FIG. 5. (a) Force-displacement data for a series of T_c measurements for sample 3. The markers indicate points where the temperature was ramped from 68 K to below T_c and then back to 68 K at fixed strain. Between these points the displacement d was ramped at 1.5 nm/s. (b) Close-up of the data in (a), showing the probable plastic relaxation of the epoxy holding the sample as $|\sigma_a|$ became large. The numbers on each marker indicate the order in which temperature ramps were performed. (c) Force-displacement data for sample 1, before and after it was fractured under tension. As in (a), the markers indicate strains where temperature ramps were performed to measure T_c, and the lines are the strain ramps between these points. The displacement was ramped at 1.5 nm/s. (d) Same as (c), for sample 2.

APPENDIX A: MORE INFORMATION ON THE SETUP

Samples were grown using a flux method [34], producing large single crystals whose oxygen content was later adjusted to 6.67 ($T_c \approx 65$ K) by annealing under well-defined oxygen partial pressure. The large samples were mechanically de-twinned by heating under slight uniaxial stress, 50–60 MPa, to 400 °C, before being cut into smaller pieces and mechanically polished to the required dimensions for the pressure cell. Samples were mounted into the uniaxial stress cell with Stycast 2850FT epoxy, cured for 4 hours at 65 °C. The epoxy layers on both the top and bottom faces of the sample ends were ≈30 μm thick. The uniaxial stress cell employed here is described in Ref. [4].

APPENDIX B: NONELASTIC DEFORMATION OF THE EPOXY, AND ZERO-FORCE DETERMINATION

In addition to the force sensor the stress cell incorporates a displacement sensor, that measures the displacement applied to the sample and epoxy that holds it. Data from this sensor provides information on the mechanical state of the sample and epoxy. Force-displacement data from sample 3, as the applied stress approached −2 GPa at $T = 68$ K, are shown in Figs. 5(a) and 5(b). Panel (a) shows $F(d)$, where F is force and d displacement, over the entire course of measurements, including the point where the sample fractured under compression and F dropped abruptly. Panel (b) shows a close-up of $F(d)$ at high stresses, approaching the point of fracture. Here, it is seen that $F(d)$ followed a gentler slope as $|\sigma_a|$ was increased than on the return strokes. This difference is visible in, for example, the difference in the slope between the points numbered 1 and 9 in the figure, where $|\sigma_a|$ was increased

monotonically, and that between points 9 and 10, where $|\sigma_a|$ was decreased. This behavior most likely shows that the epoxy relaxes plastically as high stresses are approached. That this possible plastic flow is in the epoxy, not the sample, is shown by the data in Fig. 6, where the transition observed in sample 3 at −0.79 GPa is seen to have the same shape and temperature before and after ramping to −1.6 GPa.

We note that this smooth plastic relaxation of the epoxy is in contrast to the sharp fractures observed at 5 K in Ref. [4]. The sample mounting procedure was the same, so we hypothesize that the different behavior is due to the temperature difference.

The force sensor reading varied by ≈2 N from cool-down to cool-down, and so its zero-force reading was determined in situ by deliberately fracturing each sample after measurement,
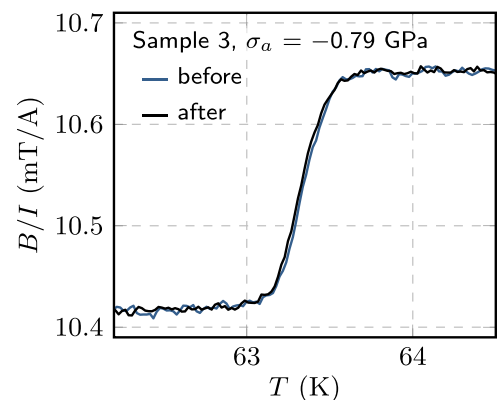

FIG. 6. Two measurements of sample 3 at $\sigma_a = -0.79$ GPa, before and after σ_a was ramped to −1.6 GPa.
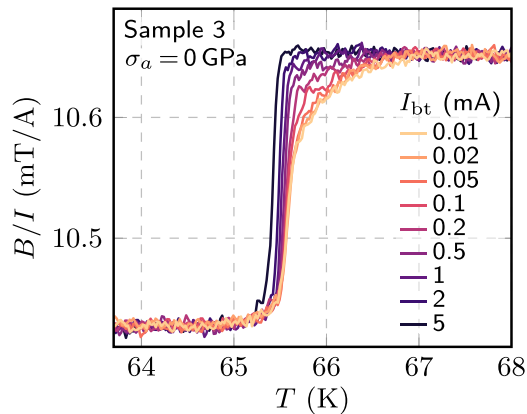
FIG. 7. The real part of the susceptometer response B/I (field in the Hall cross divided by current in the excitation coil) for different currents in the burn-through coil I_{bt}. The field from the excitation coil of the susceptometer at the sample surface was $\approx 25\ \mu T$ at 211 Hz, while the burn-through field was applied at 20 kHz. 5 mA in the burn-through coil corresponds to a field at the sample of $\approx 200\ \mu T$.
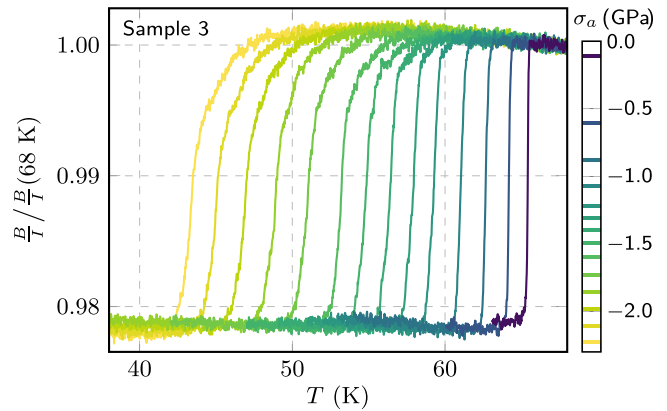

FIG. 8. Real part of the susceptometer response B/I for sample 3 at various σ_a. Due to drift, data are scaled by the readings at 68 K.

on the theory that with the sample broken, the applied force would necessarily be zero. For sample 3, the fracture was complete—a portion of the sample disappeared and the link between the two ends was completely broken, so the $F = 0$ reading could be determined with high precision. Samples 1 and 2, on the other hand, were fractured in tension, and the fractures occurred inside the epoxy, such that there remained a frictional connection between the two sample ends. $F(d)$ traces leading up to and following the fractures for samples 1 and 2 are shown in Figs. 5(c) and 5(d), respectively. For both samples, after fracture there is a portion of the force-displacement curve where the slope is strongly reduced, which we interpret as the crossover from tensile to compressive stress in the sample, rounded by frictional and plastic effects in the epoxy. Because there is no single sharp feature that can be identified as zero stress, we estimate an error of ± 0.05 GPa on the zero-stress determination for these two samples.

Although the piezoelectric actuators in the stress cell are arranged to cancel their own thermal contraction, differential thermal expansion between the main body of the cell and the sample, as well as creep and hysteresis in the actuators, can lead to changes in sample strain as the temperature is varied. For all the measurements reported here, the value of the capacitive displacement sensor was held fixed by an active feedback loop. This does not compensate for the differential thermal contraction or temperature dependence of the capacitive sensor, but over the range of temperatures studied here, 40–70 K, these effects are minimal, and the feedback does eliminate effects from creep and hysteresis in the actuators. The temperature dependence of the capacitive sensor with zero volts applied to the actuators was found to vary by 0.5 fF over this temperature range, which corresponds to a change in strain of $< 5 \times 10^{-5}$.

APPENDIX C: ADDITIONAL DATA

The effect of the "burn-through" coil is shown in Fig. 7. The width of the superconducting transition, measured with

the susceptometer, decreases from ≈ 1 to ≈ 0.1 K as the burn-through field is increased. The applied fields are negligible in comparison with the upper critical field [35], so this is an effect of inhomogeneous superconductivity. The burn-through field for all measurements with the Hall cross susceptometer shown in this paper, apart from Fig. 7, was $\approx 200\ \mu T$ at 20 kHz. The probing field from the susceptometer was $\approx 25\ \mu T$, applied at 211 Hz, for all measurements.

Susceptibility data across T_c for sample 3 are shown in Fig. 8. For this set of measurements, the signal from the Hall cross drifted over time, so data are scaled by dividing each sweep by the starting value at 68 K.

APPENDIX D: MORE INFORMATION ON THE ELASTOCALORIC EFFECT MEASUREMENTS

ECE measurements are ideally performed in the adiabatic limit, meaning that the measurement frequency should be high enough that temperature oscillations do not dissipate into the bath through the ends of the sample, yet low enough that the thermocouple thermalizes to the sample. Here, this frequency window was not broad. In analysis below, we show that at our measurement frequency of 23.11 Hz the observed signal was about 80% of its adiabatic limit. This factor is included in the normalized ECE data of Fig. 4, and the good agreement with the heat capacity jump at T_c, measured directly in Ref. [27], shows that it is at least approximately correct.

We now provide more details on the measurement. A photograph of sample 3, including the attached thermocouple, is shown in Fig. 9(a). The thermocouple is chromel-AuFe$_{0.07\%}$, and was secured to the sample with Stycast 2850FT. It was made from wire from the same spools as in Ref. [36], and we therefore apply the calibration reported there. The stress apparatus contains two sets of actuators, labeled compression and tension actuators, whose actions on the sample have opposite sign. For the ECE measurements, the compression actuators were used to apply the dc stress, and the tension actuators the ac stress, with a temperature-independent applied voltage of 1.4 V$_{rms}$. The capacitance bridge monitoring the force sensor did not have enough bandwidth for measurements at 23 Hz, and we therefore obtain a dc calibration of the tension actuator response, and, following Refs. [23,37], make the
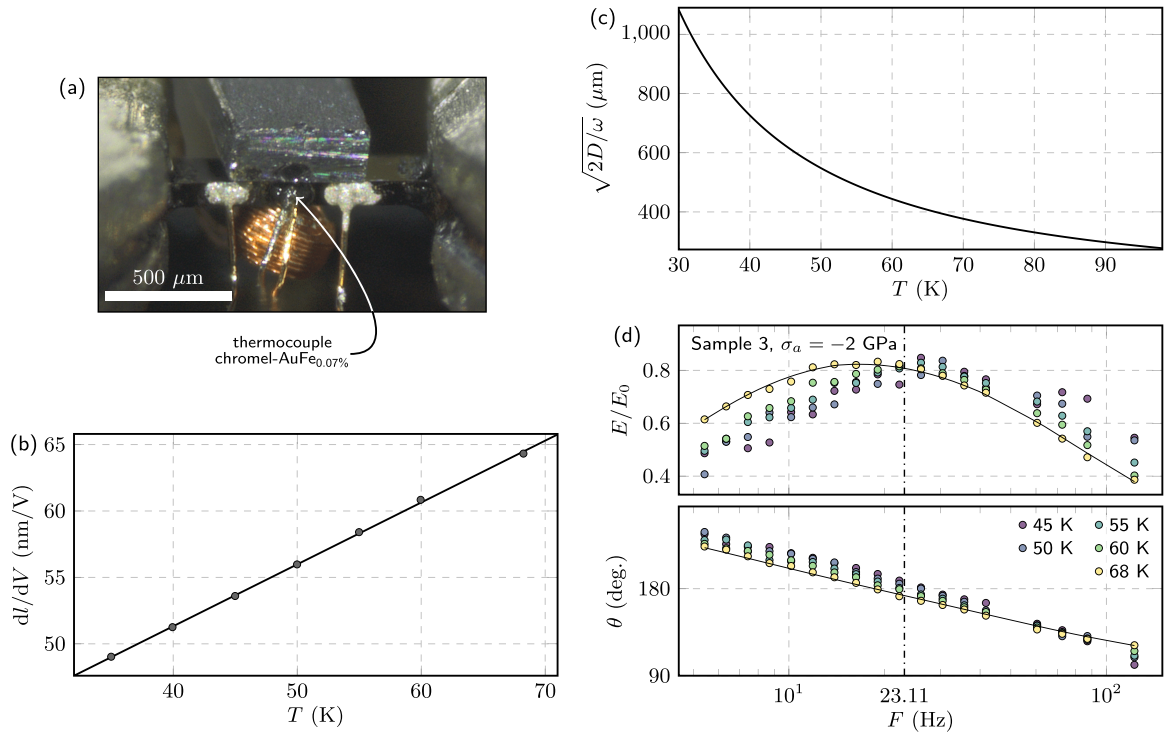
FIG. 9. (a) Micrograph of sample 3 showing the chromel-AuFe$_{0.07\%}$ thermocouple. (b) Temperature dependence of the piezoelectric actuator response to applied voltage and a linear fit to the data. (c) Temperature dependence of the characteristic thermal length of YBa$_2$Cu$_3$O$_{6.67}$ at 23.1 Hz [24]. (d) Frequency dependence of the elastocaloric effect signal, amplitude and phase, at various temperatures at $\sigma_a = -2$ GPa. The solid line is the fitted thermal transfer function at 68 K.

approximation that this calibration applies at 23 Hz. For sample 3, at $\sigma_a \sim 0$ and $T = 68$ K the stress-voltage response was 4.9 MPa/V. After the sample was fractured, we then tested the temperature response of the tension actuator by ramping the applied voltage between -10 and $+10$ V, yielding the data plotted in Fig. 9(b). Between 69 and 45 K, the actuator response decreases linearly with temperature by about 16%. We therefore take our applied ac stress to be 4.9 MPa/V $\times$ 1.4 V$_{\text{rms}} = 6.9$ MPa$_{\text{rms}}$ at 68 K, and for lower temperatures scale this by the response curve shown in Fig. 9(b).

ECE measurements yield an elastocaloric coefficient $E \equiv dT/d\sigma$. We now discuss analysis to determine E/E_0, where E_0 is the elastocaloric coefficient in the adiabatic limit. Reference [23] showed that the frequency dependence of the elastocaloric response can be well captured by a discretized thermal model. In this model,

$$\frac{E}{E_0} = (a^2 + b^2)^{-1/2}, \quad \theta = \arctan\left(\frac{a}{b}\right),$$

where θ is the phase of the signal relative to the stress oscillation, and

$$a = \frac{1}{\omega\tau_i} - \omega\tau_\theta, \quad b = 1 + \frac{C_\theta}{C_s} + \frac{\tau_\theta}{\tau_i}.$$

τ_i is the time constant for thermalization of the sample to the bath (approximated as being frequency-independent), τ_θ is that for thermalization of the temperature sensor to the sample, C_θ is the heat capacity of the sensor, and C_s is the heat capacity of the sample. We estimate C_θ/C_s, and leave τ_i and τ_θ as fitting parameters. We estimate C_θ as the heat capacity

of 700 μm of 25 μm-diameter chromel wire and 1 mm of 25-μm-diameter AuFe$_{0.07\%}$ wire, where the lengths are determined from the thermal diffusivities of these materials at 23 Hz and 65 K, in addition to a volume $150 \times 100 \times 90$ μm^3 of Stycast 2850FT. At $T = (45, 50, 55, 60, 68)$ K, we find $C_\theta \sim (0.99, 1.1, 1.3, 1.4, 1.6)$ μJ/K, and employ these values for the fitting. C_s is much larger than C_θ, and we therefore take its frequency dependence into account. Following Ref. [23], we take an approximate model in which at low frequencies C_s is the heat capacity of the entire exposed portion of the sample, and at high frequencies it is the heat capacity of a portion of the sample of length twice the thermal diffusion length ξ:

$$C_s = \begin{cases} CA_s l_{\text{exp}}, & \omega < \omega_{1D}, \\ 2CA_s\xi, & \omega > \omega_{1D}, \end{cases}$$

where C is the specific heat capacity of YBa$_2$Cu$_3$O$_{6.67}$, which we take from Ref. [27], A_s is the cross-sectional area of the sample, and $l_{\text{exp}} = 1$ mm is the exposed length of the sample. $\xi = (2D/\omega)^{1/2}$, where D is the thermal diffusivity, which we take from Ref. [24]. ω_{1D} is the angular frequency at which 2ξ crosses l_{exp}. In Fig. 9(c), we show the temperature dependence of ξ. At our measurement frequency of 23.11 Hz, we find $C_\theta/C_s \sim 0.1$ at each temperature studied here.

τ_i and τ_θ are obtained from simultaneous fitting of the observed frequency dependence of E and θ at $\sigma_a = -2.0$ GPa, where the elastocaloric response was measured against frequency. Data are shown in Fig. 9(d), along with the fitted thermal transfer function at 68 K. In the graph, E is scaled by

E_0, which is obtained from independent fitting at each temperature. The measurement frequency, 23.11 Hz, was selected as the frequency where E/E_0 is close to its maximum over the entire temperature range studied here. Based on a linear fit of E/E_0 with temperature, we find E/E_0 to vary between 0.796 at 45 K and 0.810 at 68 K. We apply this T-dependent correction to the data in Fig. 4 in the main text. Because C_θ is small, a large change in our estimate for C_θ has minimal effect. For example, doubling C_θ would reduce the maximum E/E_0 in the fitting to ~0.7.

[1] A. Steppke, L. Zhao, M. E. Barber, T. Scaffidi, F. Jerzembeck, H. Rosner, A. S. Gibbs, Y. Maeno, S. H. Simon, A. P. Mackenzie, and C. W. Hicks, Strong peak in T_c of Sr_2RuO_4 under uniaxial pressure, Science **355**, eaaf9398 (2017).

[2] C. Meingast, O. Krauf, T. Wolf, H. Wühl, A. Erb, and G. Müller-Vogt, Large $a-b$ Anisotropy of the Expansivity Anomaly at T_c in Untwinned $YBa_2Cu_3O_{7-\delta}$, Phys. Rev. Lett. **67**, 1634 (1991).

[3] U. Welp, M. Grimsditch, S. Fleshler, W. Nessler, B. Veal, and G. W. Crabtree, Anisotropic uniaxial pressure effects in $YBa_2Cu_3O_{7-\delta}$, J. Supercond. **7**, 159 (1994).

[4] M. E. Barber, A. Steppke, A. P. Mackenzie, and C. W. Hicks, Piezoelectric-based uniaxial pressure cell with integrated force and displacement sensors, Rev. Sci. Instrum. **90**, 023904 (2019).

[5] G. Ghiringhelli, M. Le Tacon, M. Minola, S. Blanco-Canosa, C. Mazzoli, N. B. Brookes, G. M. De Luca, A. Frano, D. G. Hawthorn, F. He, T. Loew, M. M. Sala, D. C. Peets, M. Salluzzo, E. Schierle, R. Sutarto, G. A. Sawatzky, E. Weschke, B. Keimer, and L. Braicovich, Long-range incommensurate charge fluctuations in $(Y,Nd)Ba_2Cu_3O_{6+x}$, Science **337**, 821 (2012).

[6] B. Keimer, S. A. Kivelson, M. R. Norman, S. Uchida, and J. Zaanen, From quantum matter to high-temperature superconductivity in copper oxides, Nature (London) **518**, 179 (2015).

[7] J. Chang, E. Blackburn, A. T. Holmes, N. B. Christensen, J. Larsen, J. Mesot, R. Liang, D. A. Bonn, W. N. Hardy, A. Watenphul, M. v. Zimmermann, E. M. Forgan, and S. M. Hayden, Direct observation of competition between superconductivity and charge density wave order in $YBa_2Cu_3O_{6.67}$, Nat. Phys. **8**, 871 (2012).

[8] T. Wu, H. Mayaffre, S. Krämer, M. Horvatić, C. Berthier, W. N. Hardy, R. Liang, D. A. Bonn, and M.-H. Julien, Incipient charge order observed by NMR in the normal state of $YBa_2Cu_3O_y$, Nat. Commun. **6**, 6438 (2015).

[9] H.-H. Kim, S. M. Souliou, M. E. Barber, E. Lefrançois, M. Minola, M. Tortora, R. Heid, N. Nandi, R. A. Borzi, G. Garbarino, A. Bosak, J. Porras, T. Loew, M. König, P. J. W. Moll, A. P. Mackenzie, B. Keimer, C. W. Hicks, and M. Le Tacon, Uniaxial pressure control of competing orders in a high-temperature superconductor, Science **362**, 1040 (2018).

[10] H.-H. Kim, E. Lefrançois, K. Kummer, R. Fumagalli, N. B. Brookes, D. Betto, S. Nakata, M. Tortora, J. Porras, T. Loew, M. E. Barber, L. Braicovich, A. P. Mackenzie, C. W. Hicks, B. Keimer, M. Minola, and M. Le Tacon, Charge Density Waves in $YBa_2Cu_3O_{6.67}$ Probed by Resonant X-Ray Scattering under Uniaxial Compression, Phys. Rev. Lett. **126**, 037002 (2021).

[11] J. Chang, E. Blackburn, O. Ivashko, A. T. Holmes, N. B. Christensen, M. Hücker, R. Liang, D. A. Bonn, W. N. Hardy, U. Rütt, M. v. Zimmermann, E. M. Forgan, and S. M. Hayden, Magnetic field controlled charge density wave coupling in underdoped $YBa_2Cu_3O_{6+x}$, Nat. Commun. **7**, 11494 (2016).

[12] S. Gerber, H. Jang, H. Nojiri, S. Matsuzawa, H. Yasumura, D. A. Bonn, R. Liang, W. N. Hardy, Z. Islam, A. Mehta, S. Song, M. Sikorski, D. Stefanescu, Y. Feng, S. A. Kivelson, T. P. Devereaux, Z.-X. Shen, C.-C. Kao, W.-S. Lee, D. Zhu *et al.*, Three-dimensional charge density wave order in $YBa_2Cu_3O_{6.67}$ at high magnetic fields, Science **350**, 949 (2015).

[13] H. Jang, W.-S. Lee, H. Nojiri, S. Matsuzawa, H. Yasumura, L. Nie, A. V. Maharaj, S. Gerber, Y.-J. Liu, A. Mehta, D. A. Bonn, R. Liang, W. N. Hardy, C. A. Burns, Z. Islam, S. Song, J. Hastings, T. P. Devereaux, Z.-X. Shen, S. A. Kivelson *et al.*, Ideal charge-density-wave order in the high-field state of superconducting YBCO, Proc. Natl. Acad. Sci. USA **113**, 14645 (2016).

[14] D. LeBoeuf, S. Krämer, W. N. Hardy, R. Liang, D. A. Bonn, and C. Proust, Thermodynamic phase diagram of static charge order in underdoped $YBa_2Cu_3O_y$, Nat. Phys. **9**, 79 (2013).

[15] J. E. Hoffman, E. W. Hudson, K. M. Lang, V. Madhavan, H. Eisaki, S. Uchida, and J. C. Davis, A four unit cell periodic pattern of quasi-particle states surrounding vortex cores in $Bi_2Sr_2CaCu_2O_{8+\delta}$, Science **295**, 466 (2002).

[16] K. Matsuba, S. Yoshizawa, Y. Mochizuki, T. Mochikua, K. Hirata, and N. Nishida, Anti-phase modulation of electron- and hole-like states in vortex core of $Bi_2Sr_2CaCuO_x$ probed by scanning tunneling spectroscopy, J. Phys. Soc. Jpn. **76**, 063704 (2007).

[17] S. A. Kivelson, D.-H. Lee, E. Fradkin, and V. Oganesyan, Competing order in the mixed state of high-temperature superconductors, Phys. Rev. B **66**, 144516 (2002).

[18] R. Okazaki, H. Shishido, T. Shibauchi, M. Konczykowski, A. Buzdin, and Y. Matsuda, High-field superconducting transition of $CeCoIn_5$ studied by local magnetic induction measurements, Phys. Rev. B **76**, 224529 (2007).

[19] C. W. Hicks, T. M. Lippman, M. E. Huber, J. G. Analytis, J.-H. Chu, A. S. Erickson, I. R. Fisher, and K. A. Moler, Evidence for a Nodal Energy Gap in the Iron-Pnictide Superconductor LaFePO from Penetration Depth Measurements by Scanning SQUID Susceptometry, Phys. Rev. Lett. **103**, 127003 (2009).

[20] S. Kittaka, H. Taniguchi, S. Yonezawa, H. Yaguchi, and Y. Maeno, Higher-T_c superconducting phase in Sr_2RuO_4 induced by uniaxial pressure, Phys. Rev. B **81**, 180510(R) (2010).

[21] J. Metzger, T. Weber, W. Fietz, K. Grube, H. Ludwig, T. Wolf, and H. Wühl, Separation of the intrinsic pressure effect on T_c of $YBa_2Cu_3O_{6.7}$ from a T_c enhancement caused by pressure-induced oxygen ordering, Physica C **214**, 371 (1993).

[22] W. H. Fietz, J. Metzger, T. Weber, K. Grube, and H. A. Ludwig, Dependence of the intrinsic dT_c/dp of $YBa_2Cu_3O_x$ on the oxygen content and the additive T_c increase by pressure-induced oxygen ordering, in *High-Pressure Science and Technology—1993*, edited by S. C. Schmidt, J. W. Shaner, G. A. Samara, and M. Ross, AIP Conf. Proc. No. 309 (AIP, New York, 1994), p. 703, https://doi.org/10.1063/1.46430.

[23] M. S. Ikeda, J. A. W. Straquadine, A. T. Hristov, T. Worasaran, J. C. Palmstrom, M. Sorensen, P. Walmsley, and I. R. Fisher, AC elastocaloric effect as a probe for thermodynamic signatures of continuous phase transitions, Rev. Sci. Instrum. **90**, 083902 (2019).

[24] J. Zhang, E. M. Levenson-Falk, B. J. Ramshaw, D. A. Bonn, R. Liang, W. N. Hardy, S. A. Hartnoll, and A. Kapitulnik, Anomalous thermal diffusivity in underdoped YBa$_2$Cu$_3$O$_{6+x}$, Proc. Natl. Acad. Sci. USA **114**, 5378 (2017).

[25] C. Krüger, K. Conder, H. Schwer, and E. Kaldis, The dependence of the lattice parameters on oxygen content in orthorhombic YBa$_2$Cu$_3$O$_{6+x}$: A high precision reinvestigation of near equilibrium samples, J. Solid State Chem. **134**, 356 (1997).

[26] M. Lei, J. L. Sarrao, W. M. Visscher, T. M. Bell, J. D. Thompson, A. Migliori, U. W. Welp, and B. W. Veal, Elastic constants of a monocrystal of superconducting YBa$_2$Cu$_3$O$_{7-\delta}$, Phys. Rev. B **47**, 6154 (1993).

[27] J. W. Loram, K. A. Mirza, J. R. Cooper, and W. Y. Liang, Electronic Specific Heat of YBa$_2$Cu$_3$O$_{6+x}$ from 1.8 to 300 K, Phys. Rev. Lett. **71**, 1740 (1993).

[28] J. D. Jorgensen, S. Pei, P. Lightfoot, D. G. Hinks, B. W. Veal, B. Dabrowski, A. P. Paulikas, R. Kleb, and I. D. Brown, Pressure-induced charge transfer and dT_c/dp in YBa$_2$Cu$_3$O$_{7-x}$, Physica C **171**, 93 (1990).

[29] J. J. Neumeier and H. A. Zimmermann, Pressure dependence of the superconducting transition temperature of YBa$_2$Cu$_3$O$_7$ as a function of carrier concentration: A test for a simple charge-transfer model, Phys. Rev. B **47**, 8385 (1993).

[30] O. Cyr-Choinière, D. LeBoeuf, S. Badoux, S. Dufour-Beauséjour, D. A. Bonn, W. N. Hardy, R. Liang, D. Graf, N. Doiron-Leyraud, and L. Taillefer, Sensitivity of T_c to pressure and magnetic field in the cuprate superconductor YBa$_2$Cu$_3$O$_y$: Evidence of charge-order suppression by pressure, Phys. Rev. B **98**, 064513 (2018).

[31] R. Liang, D. A. Bonn, and W. N. Hardy, Evaluation of CuO$_2$ plane hole doping in YBa$_2$Cu$_3$O$_{6+x}$ single crystals, Phys. Rev. B **73**, 180505(R) (2006).

[32] W. E. Pickett, Uniaxial Strain Dependence of T_c in YBa$_2$Cu$_3$O$_7$: Internal Strain Induced Intralayer Charge Transfer, Phys. Rev. Lett. **78**, 1960 (1997).

[33] J. Choi, O. Ivashko, E. Blackburn, R. Liang, D. A. Bonn, W. N. Hardy, A. T. Holmes, N. B. Christensen, M. Hücker, S. Gerber, O. Gutowski, U. Rütt, M. v. Zimmermann, E. M. Forgan, S. M. Hayden, and J. Chang, Spatially inhomogeneous competition between superconductivity and the charge density wave in YBa$_2$Cu$_3$O$_{6.67}$, Nat. Commun. **11**, 990 (2020).

[34] C. T. Lin, W. Zhou, W. Y. Liang, E. Schönherr, and H. Bender, Growth of large and untwinned single crystals of YBCO, Physica C **195**, 291 (1992).

[35] G. Grissonnanche, O. Cyr-Choinière, F. Laliberté, S. René de Cotret, A. Juneau-Fecteau, S. Dufour-Beauséjour, M.-È. Delage, D. LeBoeuf, J. Chang, B. J. Ramshaw, D. A. Bonn, W. N. Hardy, R. Liang, S. Adachi, N. E. Hussey, B. Vignolle, M. Proust, C. amd Sutherland, S. Krämer, J.-H. Park, D. Graf *et al.*, Direct measurement of the upper critical field in cuprate superconductors, Nat. Commun. **5**, 3280 (2014).

[36] U. Stockert and N. Oeschler, Thermopower of chromel–AuFe$_{0.07\%}$ thermocouples in magnetic fields, Cryogenics **51**, 154 (2011).

[37] PI Ceramic GmbH, Lindenstraße, 07589 Lederhose, Germany.

[38] Raw data available at https://doi.org/10.17617/3.IN2TYH.